

# Characterization and Strain-Hardening Behavior of Friction Stir-Welded Ferritic Stainless Steel

Gaurav Sharma, Dheerendra Kumar Dwivedi, and Pramod Kumar Jain

(Submitted October 22, 2016; in revised form September 30, 2017; published online October 27, 2017)

In this study, friction stir-welded joint of 3-mm-thick plates of 409 ferritic stainless steel (FSS) was characterized in light of microstructure, x-ray diffraction analysis, hardness, tensile strength, ductility, corrosion and work hardening properties. The FSW joint made of ferritic stainless steel comprises of three distinct regions including the base metal. In stir zone highly refined ferrite grains with martensite and some carbide precipitates at the grain boundaries were observed. X-ray diffraction analysis also revealed precipitation of  $\text{Cr}_{23}\text{C}_6$  and martensite formation in heat-affected zone and stir zone. In tensile testing of the transverse weld samples, the failure eventuated within the gauge length of the specimen from the base metal region having tensile properties overmatched to the as-received base metal. The tensile strength and elongation of the longitudinal (all weld) sample were found to be 1014 MPa and 9.47%, respectively. However, in potentiodynamic polarization test, the corrosion current density of the stir zone was highest among all the three zones. The strain-hardening exponent for base metal, transverse and longitudinal (all weld) weld samples was calculated using various equations. Both the transverse and longitudinal weld samples exhibited higher strain-hardening exponents as compared to the as-received base metal. In Kocks–Mecking plots for the base metal and weld samples at least two stages of strain hardening were observed.

**Keywords** corrosion, microstructure, stainless steel, strain hardening, tensile properties

## 1. Introduction

Ferritic stainless steels are most commonly used for manufacturing the coal carriages, construction industries and in exhaust manifolds (Ref 1, 2). In comparison with the austenitic stainless steel, they are cheaper alternative. Generally, ferritic stainless steel is welded by various conventional welding processes like gas tungsten arc welding and gas metal arc welding. However, in conventional welding of ferritic stainless steel, problems like grain coarsening in heat-affected zone, solidification cracking and segregation of alloying elements may occur which in turn result in poor weld performance (Ref 3–5). To overcome these problems feasibility of low heat input process like friction welding, diffusion bonding and friction stir welding is recommended. Friction stir welding is a practice that joins the materials by intermixing in solid state. Researchers have successfully joined the materials like aluminum, copper, steel and titanium by friction stir welding (Ref 6–9). Ahn et al. (Ref 2) carried out friction stir welding of 3-mm-thick 409L stainless steel plates using  $\text{Si}_3\text{N}_4$  tool. It was reported that no Cr-rich carbide precipitates were formed at the grain boundary in all the three zones. The tensile property of the weld joint was found to be superior to the base metal. Cheng et al. (Ref 10) investigated the friction stir

welding of low carbon steel to ductile iron using a tungsten alloy tool. Refined grains of pearlite and martensite were observed in the stir zone. Cho et al. (Ref 11) studied the friction stir-welded joint made of 2-mm-thick ferritic stainless steel plates and reported highly refined grain structure in the stir zone. The weld joint developed using ferritic stainless steel is sensitive to intergranular corrosion because of the influence of reactive ions such as  $\text{Cl}^-$ ,  $\text{SO}_4^{2-}$ ,  $\text{Br}^-$ ,  $\text{CO}_3^{2-}$  and some organic acids (Ref 12, 13). Lakshminarayanan et al. (Ref 14) investigated the sensitization behavior of 409M stainless steel and found higher degree of sensitization and corrosion rate for heat-affected zone and stir zone as compared to the base metal. Li et al. (Ref 15) carried out friction stir welding of high nitrogen nickel-free austenitic stainless steel and reported that due to the precipitation of  $\text{Cr}_{23}\text{C}_6$  in the stir zone, its corrosion resistance was lower than the base metal. The published literature provides basic knowledge about the friction stir welding of the high melting temperature materials. However, the effect of friction stir welding on strain-hardening and corrosion behavior of the ferritic stainless steel still need to be explored. Therefore, in the present work efforts were made to characterize the friction stir welding joint in light of microstructural study, mechanical properties, corrosion and work hardening aspect.

## 2. Experimental Details

### 2.1 Materials and Welding Process

For friction stir welding experiments, 3-mm-thick ferritic stainless steel plates of composition (C-0.025, Si-0.51, Mn-0.82, P < 0.005, S-0.018, Cr-10.8, Ni-1.5, Mo-0.023 and Fe-balance) were used. The plates to be weld were machined to a dimension of 150 mm × 50 mm × 3 mm, and the butting edges of the plates were surface grinded for joining purpose. Prior to

Gaurav Sharma, Dheerendra Kumar Dwivedi, and Pramod Kumar Jain, Department of Mechanical and Industrial Engineering, Indian Institute of Technology Roorkee, Roorkee, Uttarakhand 247667, India. Contact e-mails: gauraviitr1992@gmail.com and gaur8.dme2014@iitr.ac.in.

the welding, plates were placed rigidly on the machine bed with the help of fixture and wiped with acetone in order to make the faying surface free from dust, dirt, grease and other contaminations. A non-consumable tungsten carbide tool (Fig. 1a, b) was used for welding. The process parameters were optimized by trial experiments, and defect-free joints were obtained at a fixed tool tilt angle of  $1^\circ$ , tool rotational speed of 508 rpm and 20 mm/min traverse speed. Figure 1(c) represents the photograph of welded plate developed at optimized process parameters free from any surface defect. During welding, to avoid the deformation of tool material due to high temperature, a jet of compressed air was used for cooling of the tool.

## 2.2 Characterization of the Weld Joint

The microstructural properties of the welded joint were characterized in light of optical microscopy, field emission scanning electron microscopy and x-ray diffraction analysis. Slices from the welded plate were prepared, and the transverse section of the joint was wet polished using silicon carbide emery papers up to 1500 grit size and finally cloth polished using  $\text{Al}_2\text{O}_3$  polishing powder. For structural analysis, the polished samples were etched using Vilella solution. A dewinter LT-23B optical microscope and quanta-200 field emission scanning electron microscope were used to reveal the structural features of the various zones. The Vickers microhardness profile was developed on the transverse section of the joint. The hardness was measured at the transverse section at midthickness of the welded plate using 200-g load and 10-s

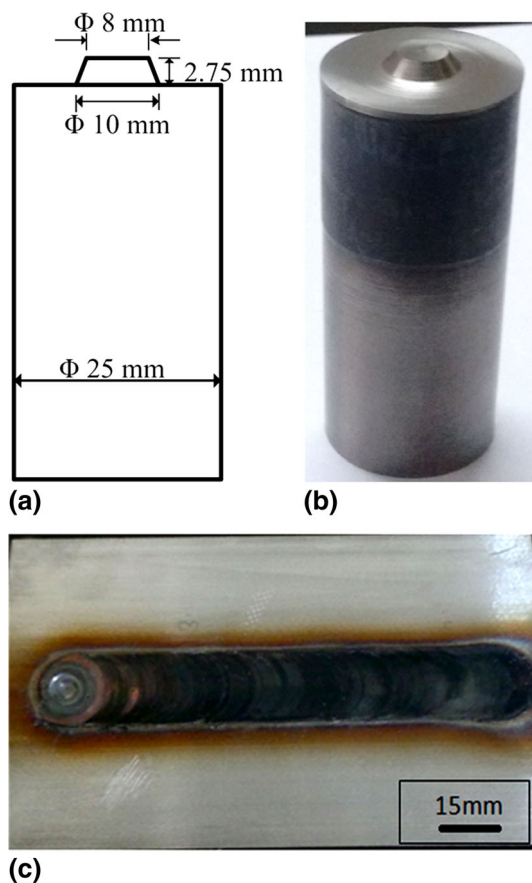


**Fig. 1** (a) Schematic of tool design, (b) tungsten carbide tool used for welding and (c) welded plates free from any surface defects

dwelt time in such a way that the distance between two consecutive Vickers indents was 1 mm. The tensile specimen of the base metal and weld joint was prepared according to ASTM E8. The tensile testing was done using a vertical Instron tensile testing machine at strain rate of  $6.66 \times 10^{-4} \text{ s}^{-1}$ . Further, the detailed study of fractured surface of the tensile test specimen was carried out using scanning electron microscopy.

## 2.3 Corrosion Experiments

For corrosion experiments, the slices from the welded plates were machined and mounted with epoxy resin (Fig. 2a). The potentiodynamic polarization test was carried out to examine the electrochemical behavior of the various zones of the weld joint. The transverse section of the weld joint was polished with the help of silicon carbide papers up to 1500 grit size and then using polishing cloth. All the samples were cleaned with acetone and dried by hot air prior to the testing. The portion of the specimen next to the exposed area was masked with the help of a solution containing nitrocellulose and butyl acetate (Fig. 2b). During the test, the epoxy-mounted samples, saturated calomel electrode and graphite rod electrode were used as the working, reference and counter electrode, respectively. Corrosion testing was carried out using Gamry's 'Interface 1000' potentiostat and the DC 105 software. Figure 2(c) and (d) represents the corrosion test setup and the schematic of electrolytic cell used for the corrosion testing. All tests were performed in 3.5% NaCl solution at room temperature ( $25 \pm 2^\circ \text{C}$ ), and the potential was swept from  $-1.5$  to  $1 \text{ V}$  with  $1 \text{ mV/s}$  scan rate. Before the test, all the samples were subjected to 1800-s open-circuit delay time to stabilize the potential.

## 3. Results and Discussion

### 3.1 Microstructure Characterization

The AISI 409 ferritic stainless steel plates of 3 mm thickness were successfully welded by friction stir welding process. The joint was free from any surface defect, indicating sufficient heat input for material flow during welding at the optimized process parameters. Microstructure of the as-received base metal mainly exhibited ferrite grains with randomly distributed carbides (Fig. 3). For the measurement of grain size in all the zones, MATLAB software was used using a line cut program. In base metal, the average grain size was found to be  $23 \mu\text{m}$ .

In microstructure analysis of the weld joint, three different regions were observed including the base metal. The optical micrographs of various regions of the friction stir-welded joint are shown in Fig. 4. The microstructure of the heat-affected zone was influenced by heat generated during friction stir welding. In heat-affected zone region recrystallized ferritic grains, carbide precipitates and small fraction of martensite were observed (Fig. 4b, c). The average size of ferrite grains was reduced to  $20 \mu\text{m}$  in this region. A typical thermomechanical-affected zone (TMAZ), which forms between heat-affected zone and stir zone, was not observed in the present study. Similar kind of findings was also reported by Lienert et al. (Ref 16) in friction stir welding of steels. In microstructure study of the stir zone, no major changes were observed from top to bottom of the stir zone (Fig. 4d, e). The temperature of

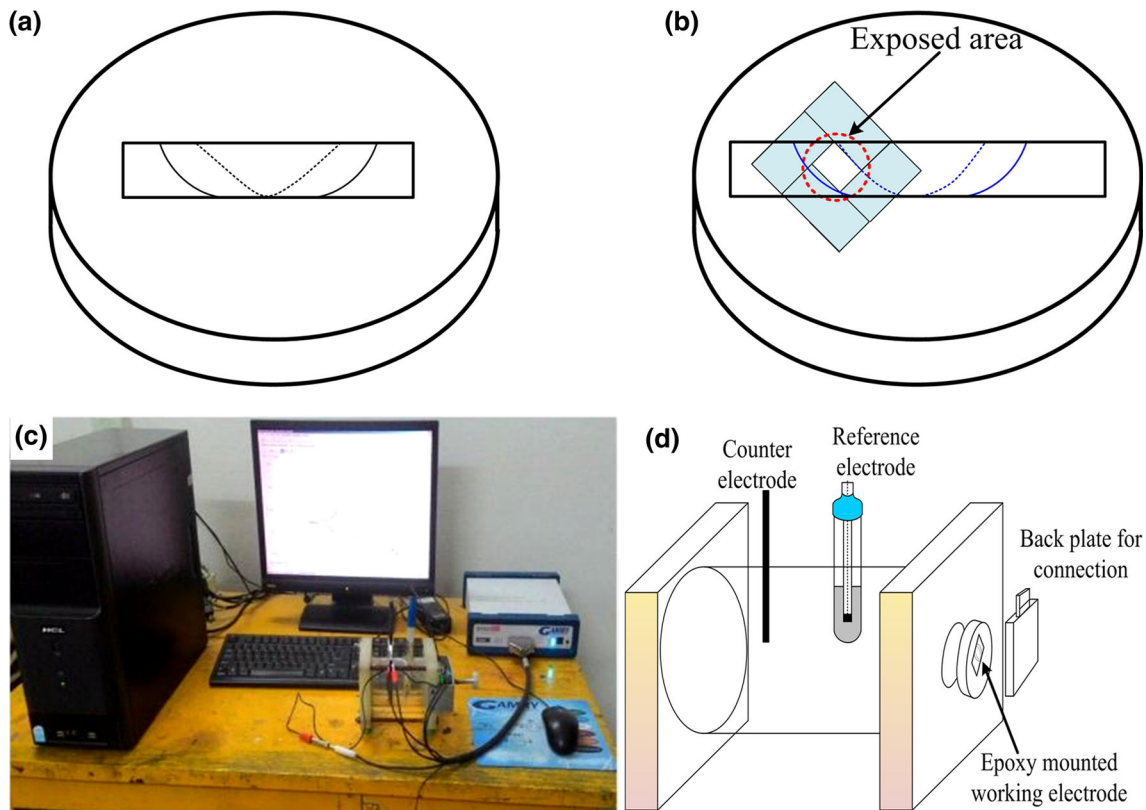


**Fig. 2** (a) Schematic of epoxy-mounted specimen, (b) masking of the specimen, (c) corrosion test setup and (d) schematic of electrolytic cell

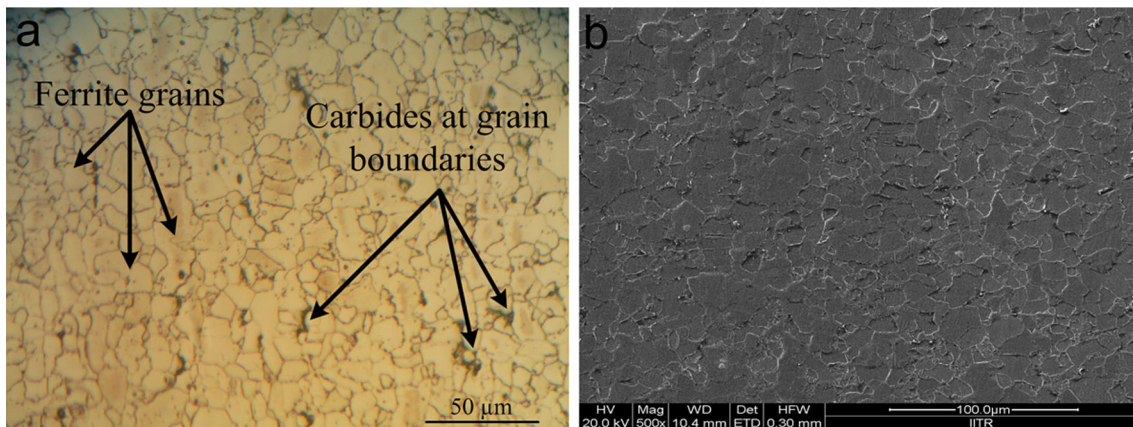


**Fig. 3** Micrograph of as-received base metal captured by: (a) optical microscope and (b) FE-SEM

the stir zone was expected to be more than 1000 °C during FSW of steel (Ref 17). Therefore, the material in this region underwent both the thermal and mechanical cycles, which in turn led to microstructural modification in form of grain refinement due to recrystallization. The microstructure of the stir zone was characterized by the presence of carbides and martensite at the grain boundary region of the highly refined equiaxed ferritic grains. The micrographs taken by the scanning electron microscope in heat-affected zone and stir zone of FSW joint are presented in Fig. 5(a) and (b). X-ray diffraction analysis was performed to identify the various phases formed during welding. XRD peaks also confirmed the presence of these phases in various zones of the FSW joint (Fig. 6).

The grain refinement in stir zone could be explained with the help of dynamic recrystallization. The dynamic recrystallization may occur discontinuously or continuously. In discontinuous dynamic recrystallization, new grain nucleates at old high-angle grain boundaries, whereas continuous dynamic recrystallization is characterized by increasing misorientation of existing subgrain boundaries. Ferritic stainless steel and Al alloys generally undergo continuous dynamic recrystallization because they possess high stacking fault energy (Ref 18). The maximum peak intensity of each phase obtained from x-ray diffraction analysis was utilized to analyze various phase products during friction stir welding. The normalized intensity ratio (NIR) of various phases was calculated using Eq 1.

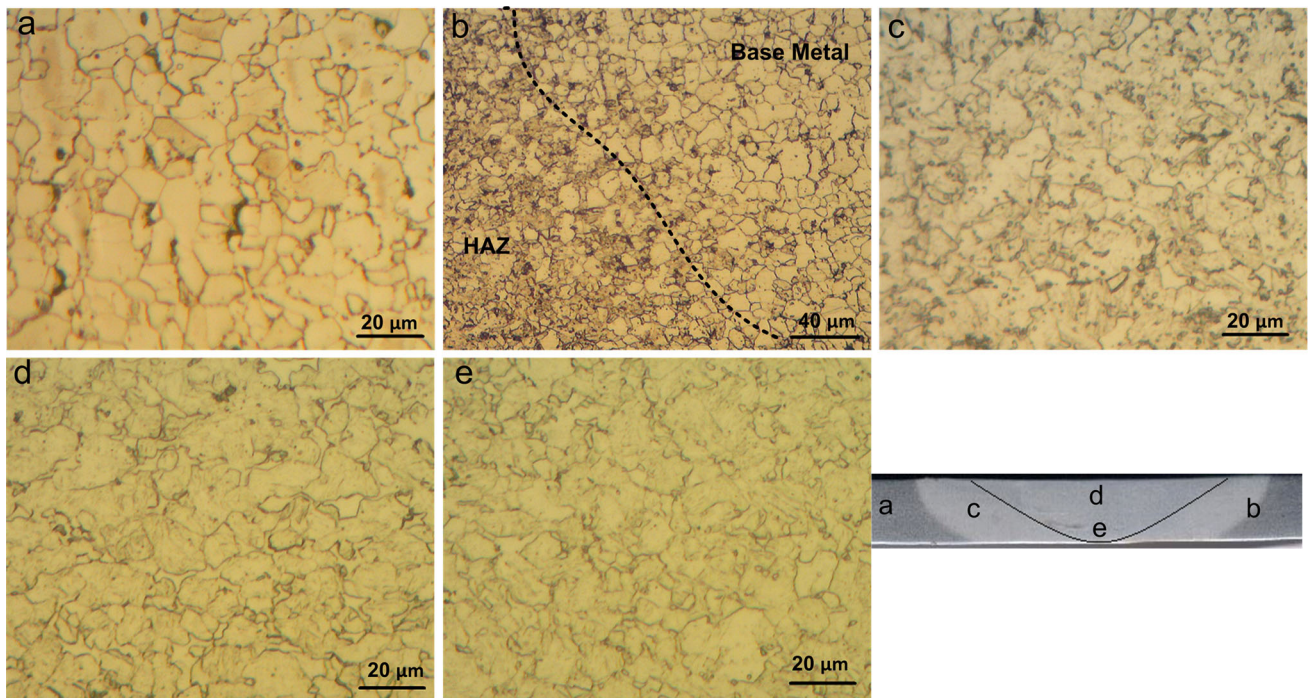


Fig. 4 Optical micrographs of various points in each zone of FSW joint

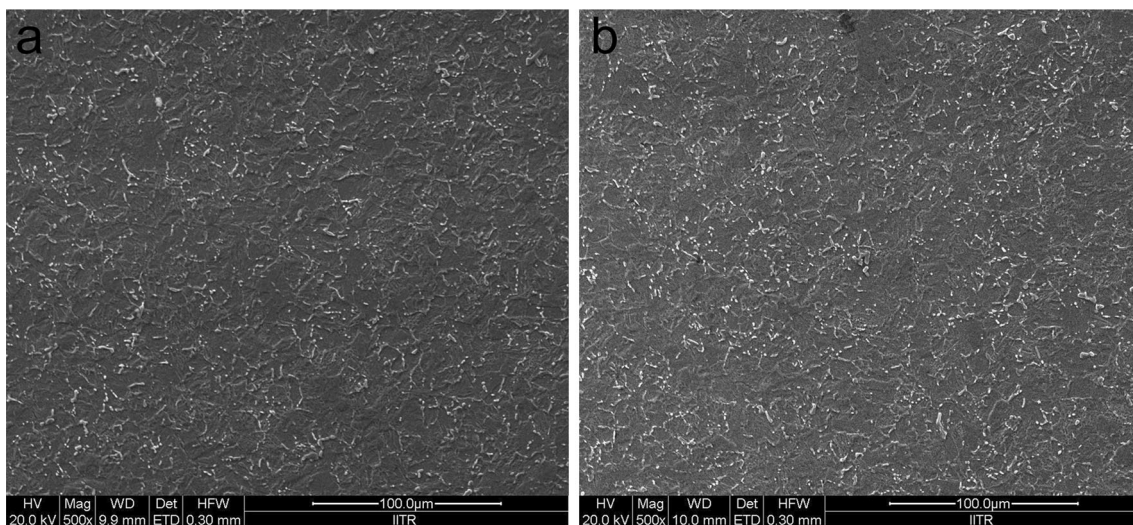


Fig. 5 SEM micrograph of: (a) heat-affected zone and (b) stir zone

$$(\text{NIR})_{\alpha} = \frac{I_{\alpha} - I_{\text{back}}}{\sum_{\alpha=1}^n I_{\alpha} - nI_{\text{back}}} \quad (\text{Eq 1})$$

where  $I_{\alpha}$  is the intensity of  $\alpha$  phase and  $I_{\text{back}}$  is the background intensity. The calculated values of NIR for various phases present in each region are given in Table 1. For finding the intensities of various phases, only dominating peaks in the x-ray diffraction pattern were considered.

### 3.2 Mechanical Properties

The microhardness profile was developed by measuring the Vickers hardness at the middle of the transverse section of the joint as a function of distance and is shown in Fig. 7. The

microhardness of the as-received base metal was measured as  $220 \pm 5$  HV. Next to the base metal, heat-affected zone existed where the hardness was in the range of 267-360 HV. This increase in the hardness value in this region was due to the grain refinement and the formation of the martensite. At the center, i.e., stir zone, the hardness was found in the range of 324-467 HV. On the basis of microhardness profile, the stir zone possessed the highest hardness. It was observed that the hardness of the weld joint increased due to the increase in martensite content in heat-affected zone and stir zone. However, from base metal to the stir zone, a large scatter was found in the hardness values. This scatter in the hardness was due to the presence of metallurgical heterogeneity and formation of martensite in heat-affected zone and stir zone at the grain boundaries.

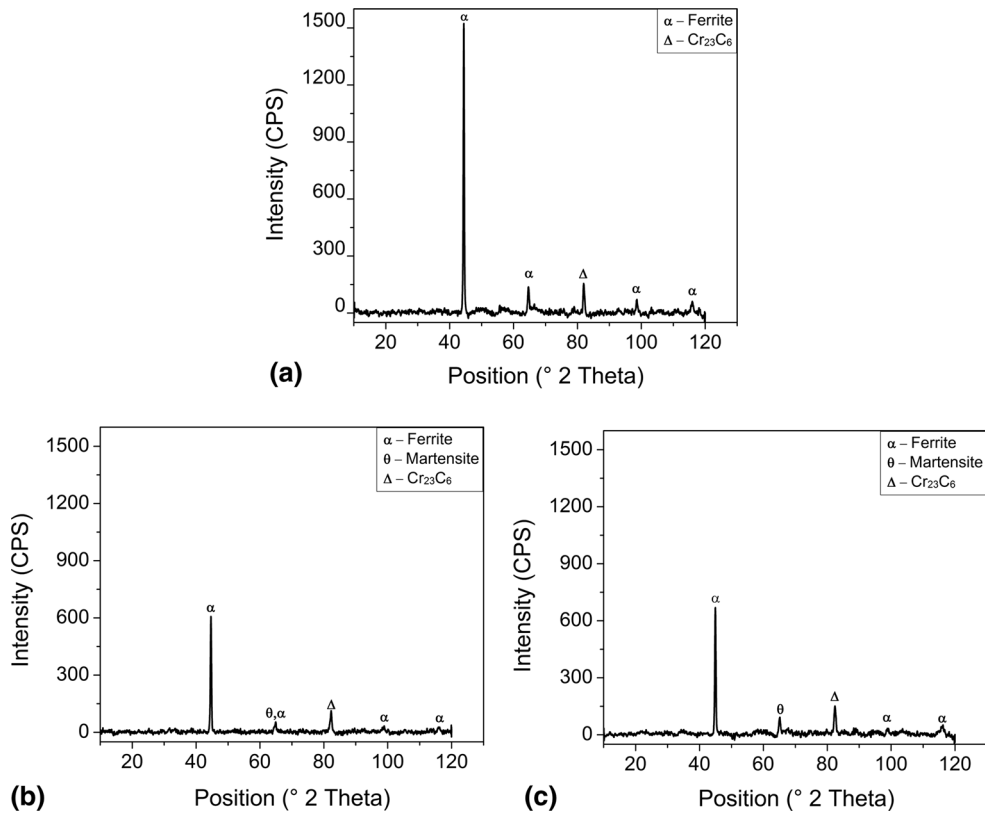


Fig. 6 X-ray diffraction patterns of (a) base metal, (b) heat-affected zone and (c) stir zone

Table 1 Calculated NIR for various phases present in base metal, heat-affected zone and stir zone

| Specimen   | Phase    | $I_1$ | $I_2$ | $I_3$ | $I_{back}$ | NIR, % |
|------------|----------|-------|-------|-------|------------|--------|
| Base metal | $\alpha$ | 1523  | ...   | ...   | 4          | 91.28  |
|            | $\Delta$ | ...   | 149   | ...   | 4          | 8.71   |
| HAZ        | $\alpha$ | 607   | ...   | ...   | 8          | 79.86  |
|            | $\Delta$ | ...   | 113   | ...   | 8          | 14.00  |
|            | $\theta$ | ...   | ...   | 54    | 8          | 6.13   |
| Stir zone  | $\alpha$ | 669   | ...   | ...   | 3          | 73.75  |
|            | $\Delta$ | ...   | 151   | ...   | 3          | 16.39  |
|            | $\theta$ | ...   | ...   | 92    | 3          | 9.85   |

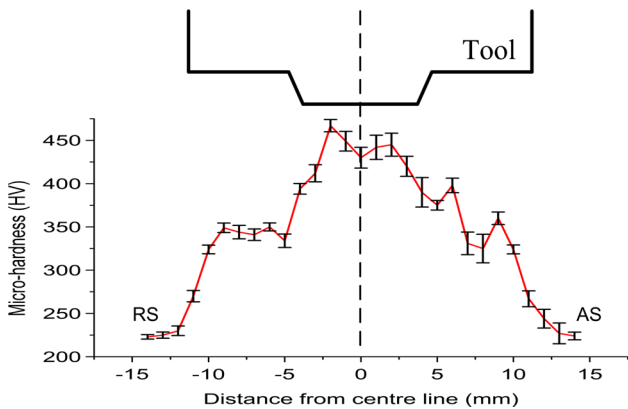


Fig. 7 Microhardness profile of friction stir-welded joint at midthickness of transverse section

Tensile tests were conducted on both as-received base metal and transverse specimens prepared from weldment. Two samples for each condition were prepared, and the average value was reported. The yield strength, ultimate tensile strength and ductility of the as-received base metal were found to be 310.8, 504.3 MPa and 22.2%, respectively. The weld metal was found to be stronger than the base metal. However, there was a reduction in the % elongation in the weldments (11.73%) as compared to the as-received base metal (22.23%). The yield strength of the transverse weld samples (330.29 MPa) was found to be higher than the base metal (310.84 MPa). The welded samples were failed from the base metal side within the gauge length of tensile specimen which in turn gives tensile strength value similar to that of as-received base metal, from the ultimate tensile strength obtained by tensile testing; the weld efficiency was calculated using Eq 2.

### Weld efficiency

$$= \frac{\text{Ultimate tensile strength of the weld joint}}{\text{Ultimate tensile strength of the as-received base metal}} \quad (\text{Eq 2})$$

The joint efficiency in transverse weld condition was found to be 101.2%. In tensile testing of the transverse weld samples fracture occurred from the base metal, so longitudinal (all weld) tensile specimens were prepared to evaluate the strength and ductility of the stir zone. Tensile properties of all the specimens are summarized in Table 2, and the engineering stress–strain behavior of the specimen taken from both transverse and longitudinal (all welds) directions of welding is represented in Fig. 8. It could be clearly seen that the tensile strength of longitudinal weld samples (1014.2 MPa) was much higher than the as-received base metal (504.3 MPa) and transverse weld samples (510.6 MPa).

The improvement in the yield and tensile strength of the all weld samples was due to the formation of martensite and carbide precipitation in stir zone after FSW as evident from normalized intensity ratio analysis obtained from x-ray diffraction analysis (Table 1). The stir zone has 9.85 and 16.39% martensite and carbide precipitates, respectively. The yield and ultimate tensile strength were found to be increased with increase in volume fraction of martensite (Ref 19). Hence, the yield and tensile strength of the longitudinal (all weld) samples were much higher than the base metal, which also resulted in increase in hardness as well as reduction in ductility.

### 3.3 Strain-Hardening Behavior

To understand the strain-hardening behavior of the as-received base metal and welded samples, the strain-hardening exponents were calculated using Eq 3-5.

$$\sigma = K\varepsilon^n \quad (\text{Eq 3})$$

$$\sigma = \sigma_y + K_1\varepsilon^{n_1} \quad (\text{Eq 4})$$

$$\sigma = \sigma_y + K^*(\varepsilon - \varepsilon_y)^{n^*} \quad (\text{Eq 5})$$

where  $K$ ,  $K_1$  and  $K^*$  are strength coefficients and  $n$ ,  $n_1$  and  $n^*$  are the strain-hardening exponents,  $\varepsilon$  is the true strain, and  $\varepsilon_y$  is the yield strain. The calculated values of various strain-hardening exponents for as-received base metal and both types of welded samples are represented in Table 3. It was observed that  $n$  and  $n^*$  values for transverse weld samples were quite similar to the as-received base metal. On the other hand for longitudinal weld samples, all the exponent values were much higher than the as-received base metal and transverse weld joint. Further, Kocks–Mecking-type plot was plotted by plotting strain-hardening rate ( $\theta$ ) at ordinate axis and the net flow stress on the abscissa (Fig. 9).

In all the conditions, I and II hardening stages were not observed at all, but the III and IV stages were observed. In stage III, the  $\theta$  value decreases as the net flow stress increases and this stage occurs immediately after yielding. The stage IV appeared after the hardening stage III. The  $\theta$  value for all weld samples was higher than the as-received base metal. It could be explained by grain size and dislocation density. The strain-hardening rate was known to increase with grain refinement and decrease in dislocation density (Ref 20). Friction stir welding resulted in grain refinement and lowered the dislocation density due to dynamic recrystallization resulting in high  $\theta$  value.

### 3.4 Fractured Surface Analysis

In order to study the fractured surface of the tensile test specimen of the as-received base metal and welded samples, scanning electron microscopy was performed (Fig. 10). The presence of dimples at tensile-fractured surface of both base metal and longitudinal weld suggested the ductile fracture under tensile testing. Few large and deep dimples in the base metal suggested a significant elongation before failure (Fig. 10a), whereas fine and shallow dimples in case of weld joint indicated a limited elongation and high strength prior to failure (Fig. 10c). The energy-dispersive spectroscopy (EDS) analysis of fractured surface exhibited the presence of Cr, Ni, Mn, C and Fe at the crack tip of fractured surface of base metal and weld (Fig. 10b, d). The carbide precipitates at grain boundaries acted as the sites for void nucleation during tensile testing, which in turn produced very fine dimples at the grain boundaries.

### 3.5 Corrosion Resistance

In order to examine the corrosion properties of the various zones of the friction stir-welded joint, the potentiodynamic polarization test was performed in 3.5 wt.% NaCl solution. The electrochemical potentiodynamic polarization curve for base metal, heat-affected zone and stir zone of weld joint is

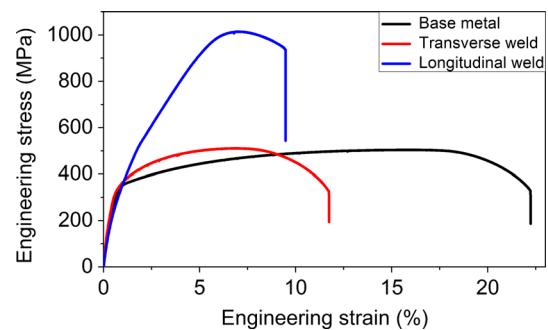


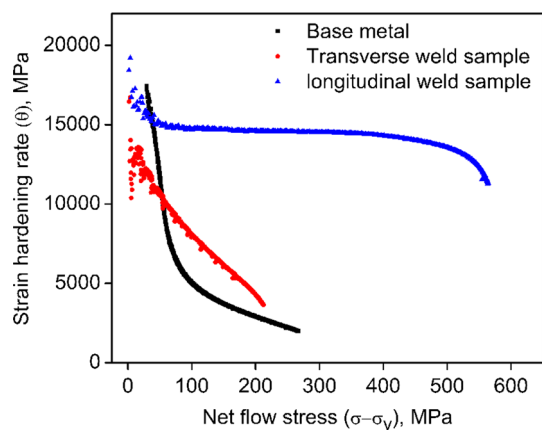
Fig. 8 Stress vs. strain curve for as-received base metal, transverse and longitudinal weld samples

Table 2 Results of the tensile test for as-received base metal and welded joint

| Specimen type     | Tensile strength, MPa | Yield strength, MPa | Elongation, % | Weld efficiency, % |
|-------------------|-----------------------|---------------------|---------------|--------------------|
| Base metal        | 504.3                 | 310.84              | 22.23         |                    |
| Transverse weld   | 510.6                 | 330.29              | 11.73         | 101.2              |
| Longitudinal weld | 1014.2                | 512.12              | 9.47          | ...                |

**Table 3 Strain-hardening exponents of the as-received base metal, longitudinal and transverse weld samples**

| Specimens                 | $n$  | $n_1$ | $n^*$ |
|---------------------------|------|-------|-------|
| Base metal                | 0.19 | 0.59  | 0.50  |
| Transverse weld samples   | 0.21 | 0.70  | 0.52  |
| Longitudinal weld samples | 0.57 | 1.46  | 0.82  |



**Fig. 9** Strain-hardening rate ( $\theta$ ) vs. net flow stress ( $\sigma - \sigma_y$ ) for base metal and welded samples at a strain rate of  $6.67 \times 10^{-4} \text{ s}^{-1}$

presented in Fig. 11. It was observed that in potentiodynamic polarization test of the base metal, the anodic current increased rapidly at a constant potential value. The increase in the current was due to the localized breakdown of the passive film by chloride ions. Generally, such breakdown of the passive film was associated with some discontinuity and led to the exposure of the underlying metal which dissolved and resulted in rapid increase in anodic current.

The values of  $E_{\text{cor}}$ ,  $I_{\text{cor}}$ ,  $\beta_a$  and  $\beta_c$  were determined and are summarized in Table 4. The  $E_{\text{cor}}$  was the potential at which the corrosion of the metal surface started. It was found that the as-received base metal showed the noblest corrosion potential of  $-406 \text{ mV}$  as well as the lowest corrosion current density of  $2.1 \mu\text{A}/\text{cm}^2$ . The corrosion potential of heat-affected zone and stir zone was  $-805$  and  $-991 \text{ mV}$ , respectively, indicating somewhat lower corrosion resistance after friction stir welding (Fig. 11). The corrosion current density for heat-affected zone and stir zone was  $9.3$  and  $14.6 \mu\text{A}/\text{cm}^2$ , respectively. From Table 4, it can be observed that the value of anodic and cathodic slope is affected by the welding process, which is attributed to that the mechanism and both anodic and cathodic reactions are affected. However, in case of base metal and stir zone, the change in the value of  $\beta_a$  was prominent as compared to the change in value of the  $\beta_c$ , which reveals that only the mechanism of the anodic reaction was affected. The corrosion rate for all the three zones was also calculated using Eq 6 (Ref 21).

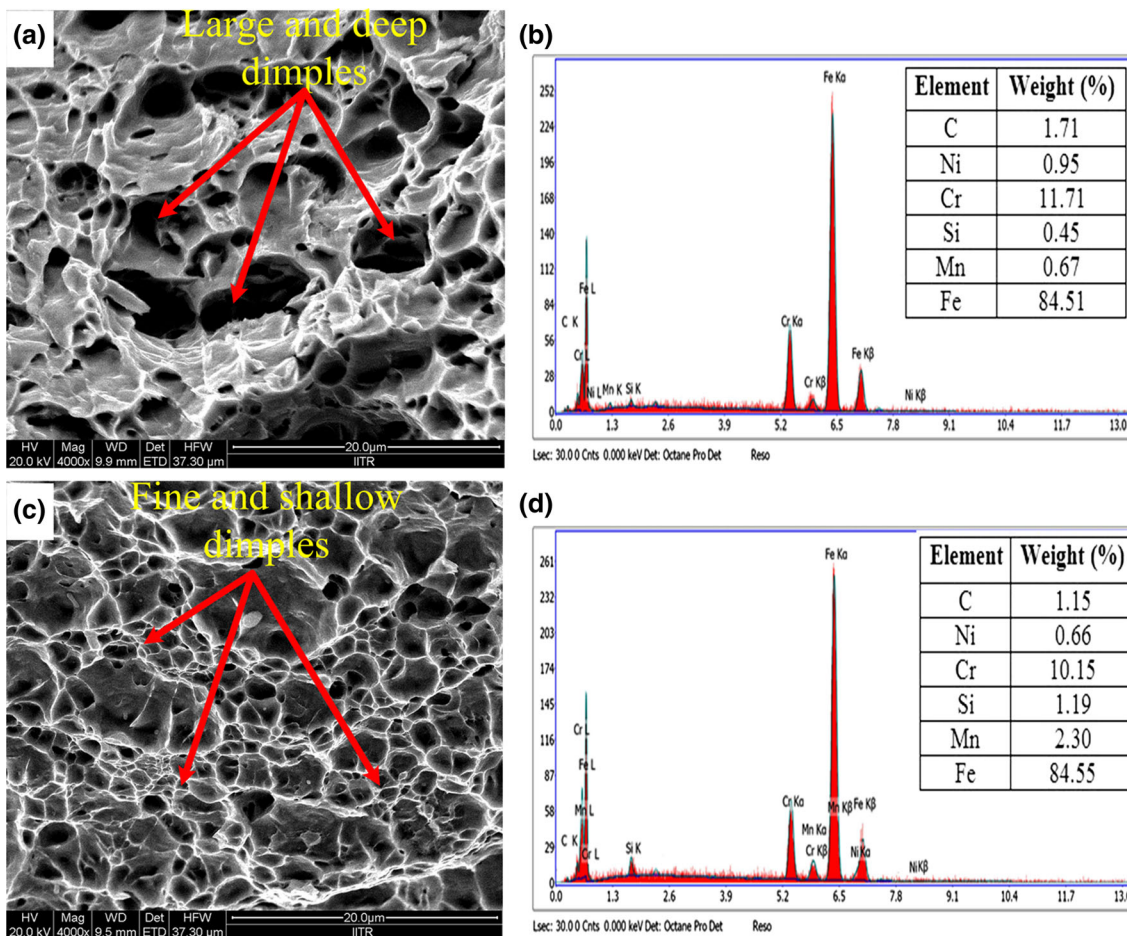


**Fig. 10** SEM fractograph and EDS spectra of tensile test specimen: (a, b) base metal and (c, d) longitudinal weld sample

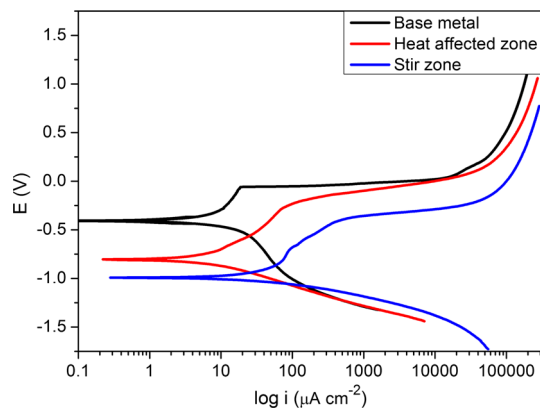


**Fig. 11** Potentiodynamic polarization curve for base metal, heat-affected zone and stir zone in 3.5 wt.% NaCl solution at room temperature

$$CR = \frac{3.27 \times 10^{-3} \times i_{\text{corr}} \times EW}{\rho} \quad (\text{Eq 6})$$

where CR is the corrosion rate in millimeter per year (mm/year);  $i_{\text{corr}}$  is the corrosion current density; EW is the equivalent weight;  $\rho$  is the density of the ferritic stainless steel. The corrosion rate of as-received base metal, heat-affected zone and stir zone was  $25 \times 10^{-3}$ ,  $111 \times 10^{-3}$  and  $176 \times 10^{-3}$  mm/year, respectively, and found to be in good agreement with  $E_{\text{corr}}$  values. The higher corrosion rate of the weld and heat-affected zone is attributed to the formation of local cell between the precipitates and the matrix. Figure 12 shows the micrographs of the exposed surface of the various zones after potentiodynamic polarization test. In all the cases large and deep pits were observed on the corroded surface. It is well known that the corrosion resistance of various zones of FSW joint is affected by the microstructural changes occurred dur-

**Table 4** Corrosion parameters and corrosion rate for the ferritic stainless steel weld tested in 3.5% NaCl solution

| Specimen           | $E_{\text{corr}}$ , mV | $i_{\text{corr}}$ , $\mu\text{A}/\text{cm}^2$ | $\beta_a$ , mV/dec | $\beta_c$ , mV/dec | Corrosion rate, mm/year |
|--------------------|------------------------|---|--------------------|--------------------|-------------------------|
| Base metal         | -406                   | 2.1   | 138.1              | 97.6               | $25 \times 10^{-3}$     |
| Heat-affected zone | -805                   | 9.3   | 708.2              | 239.0              | $111 \times 10^{-3}$    |
| Stir zone          | -991                   | 14.6  | 183.3              | 85.5               | $176 \times 10^{-3}$    |

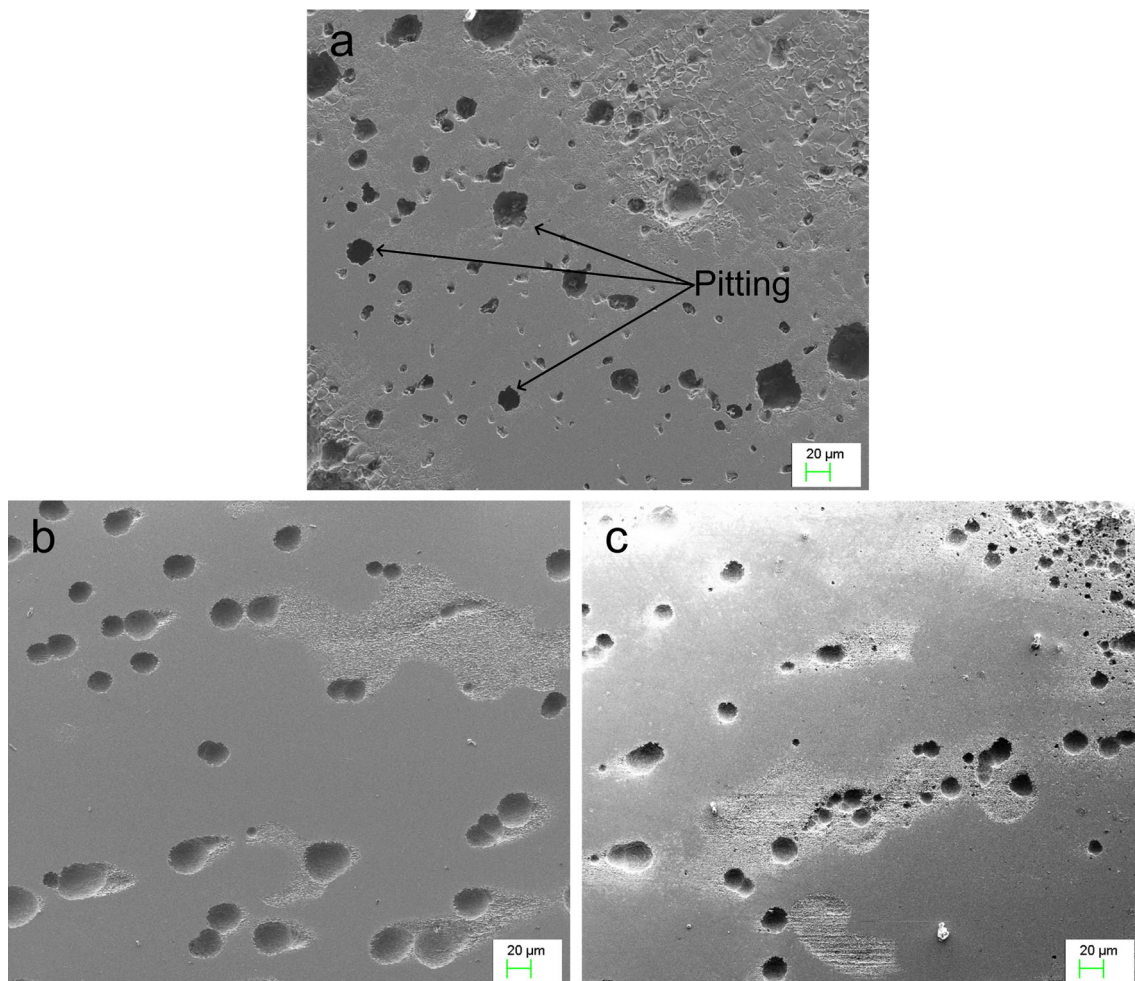


**Fig. 12** Morphologies of samples after potentiodynamic polarization test: (a) as-received base metal, (b) heat-affected zone and (c) stir zone



ing welding. Lower corrosion resistance of stir zone than heat-affected zone and base metal could be attributed to the formation of high fraction of chromium carbide as obtained from NIR analysis. Precipitates were formed in higher amount in stir zone (16.39%) as compared to base metal (8.73%) and heat-affected zone (14.0%). The precipitation of secondary phases and carbides on grain boundary increased the formation of chromium-depleted region near the grain boundary, and these chromium-depleted zones became susceptible to intergranular corrosion (Ref 15). The chromium-depleted region in the vicinity of the grain boundaries became the preferential site for corrosion when exposed to a corrosive environment. Lakshminarayanan et al. (Ref 22) also reported lower corrosion resistance of stir zone and heat-affected zone compared to the base metal. However, it was also reported that the friction stir weld joint possessed lower degree of sensitization compared to fusion welding processes.

## 4. Conclusions

In a nutshell, present work characterizes the friction stir-welded joint of 3-mm-thick ferritic stainless steel plate in light of microstructural study, mechanical characterization, corrosion and work hardening aspect. By summarizing the findings of this investigation, it can be concluded that:

1. A sound weld joint of ferritic stainless steel was acquired without any defect. The stir zone was characterized by refined grain structure with grain boundary martensite and  $\text{Cr}_{23}\text{C}_6$  precipitates based on microstructure and x-ray diffraction analysis.
2. The weld joint offers overmatched mechanical properties as compared to the base metal. The ultimate tensile strength of transverse specimen of the weld joint (510.6 MPa) was approximately similar to the base metal (504.3 MPa). However, the elongation (11.13%) was less than the base metal (22.23%).
3. Based on the polarization test, the corrosion resistance of the stir zone was found to be slightly lower than the base metal and heat-affected zone due to  $\text{Cr}_{23}\text{C}_6$  precipitation.
4. In Kocks–Mecking plots for the as-received base metal and weld samples at least two stages of strain hardening were observed having higher  $\theta$  value of the all weld samples.

## Acknowledgments

The author would like to acknowledge the support and technical help received from Shivraman Thapliyal, research scholar, in Department of Mechanical and Industrial Engineering, IIT Roorkee.

## References

1. R.S. Vidyarthi, D.K. Dwivedi, and M. Vasudevan, Influence of M-TIG and A-TIG Welding Process on Microstructure and Mechanical Behavior of 409 Ferritic Stainless Steel, *J. Mater. Eng. Perform.*, 2017, **26**, p 1391
2. B.W. Ahn, D.H. Choi, D.J. Kim, and S.B. Jung, Microstructures and Properties of Friction Stir Welded 409L Stainless Steel Using a  $\text{Si}_3\text{N}_4$  Tool, *Mater. Sci. Eng. A*, 2012, **532**, p 476
3. W. Wu, S. Hu, J. Shen, L. Ma, and J. Han, Sensitization of 21% Cr Ferritic Stainless Steel Weld Joints Fabricated With/Without Austenitic Steel Foil as Interlayer, *J. Mater. Eng. Perform.*, 2015, **24**, p 1505
4. E. Folkhard, *Welding Metallurgy of Stainless Steels*, Springer-Verlag Wien, New York, 1988
5. M.M. Husain, R. Sarkar, T.K. Pal, N. Prabhu, and M. Ghosh, Friction Stir Welding of Steel: Heat Input, Microstructure, and Mechanical Property Co-relation, *J. Mater. Eng. Perform.*, 2015, **24**, p 3673
6. A. Elrefaey, M. Gouda, M. Takahashi, and K. Ikeuchi, Characterization of Aluminum/Steel Lap Joint by Friction Stir Welding, *J. Mater. Eng. Perform.*, 2005, **14**, p 10
7. A.K. Lakshminarayanan and V. Balasubramanian, Tensile and Impact Toughness Properties of Gas Tungsten Arc Welded and Friction Stir Welded Interstitial Free Steel Joints, *J. Mater. Eng. Perform.*, 2011, **20**, p 82
8. G. Sharma and D.K. Dwivedi, Study on Microstructure and Mechanical Properties of Dissimilar Steel Joint Developed Using Friction Stir Welding, *Int. J. Adv. Manuf. Technol.*, 2017, **88**, p 1299
9. G. Sharma and D.K. Dwivedi, Structure and Properties of Friction Stir Weld Joints of Structural Steel, *Trans. Indian Inst. Met.*, 2017, **70**, p 201
10. C.P. Cheng, H.M. Lin, and J.C. Lin, Friction Stir Welding of Ductile Iron and Low Carbon Steel, *Sci. Technol. Weld. Join.*, 2010, **15**, p 706
11. H.-H. Cho, H.N. Han, S.-T. Hong, J.-H. Park, Y.-J. Kwon, S.-H. Kim, and R.J. Steel, Microstructural Analysis of Friction Stir Welded Ferritic Stainless Steel, *Mater. Sci. Eng. A*, 2011, **528**, p 2889
12. J.K. Kim, Y.H. Kim, S.H. Uhm, J.S. Lee, and K.Y. Kim, Intergranular Corrosion of Ti-Stabilized 11 wt% Cr Ferritic Stainless Steel for Automotive Exhaust Systems, *Corros. Sci.*, 2009, **51**, p 2716
13. H.B. Li, Z.H. Jiang, H. Feng, H.C. Zhu, B.H. Sun, and Z. Li, Corrosion Behavior of Ferritic Stainless Steel With 15wt% Chromium for the Automobile Exhaust System, *Int. J. Miner. Metall. Mater.*, 2013, **20**, p 850
14. A.K. Lakshminarayanan and V. Balasubramanian, Sensitization Resistance of Friction Stir Welded AISI 409 M Grade Ferritic Stainless Steel Joints, *Int. J. Adv. Manuf. Technol.*, 2012, **59**, p 961
15. H.B. Li, Z.H. Jiang, H. Feng, S.C. Zhang, L. Li, P.D. Han, R.D.K. Misra, and J.Z. Li, Microstructure, Mechanical and Corrosion Properties of Friction Stir Welded High Nitrogen Nickel-Free Austenitic Stainless Steel, *Mater. Des.*, 2015, **84**, p 291
16. T. Lienert and W.S. Jr., Friction Stir Welding Studies on Mild Steel, *Weld. J. Res. Suppl.*, 2003, **82**, p 1
17. R.S. Mishra and Z.Y. Ma, Friction Stir Welding and Processing, *Mater. Sci. Eng. R Reports*, 2005, **50**, p 1
18. A.K. Lakshminarayanan and V. Balasubramanian, An Assessment of Microstructure, Hardness, Tensile and Impact Strength of Friction Stir Welded Ferritic Stainless Steel Joints, *Mater. Des.*, 2010, **31**, p 4592
19. H.C. Chen and G.H. Cheng, Effect of Martensite Strength on the Tensile Strength of Dual Phase Steels, *J. Mater. Sci.*, 1989, **24**, p 1991
20. H. Khodaverdizadeh, A. Mahmoudi, A. Heidarzadeh, and E. Nazari, Effect of Friction Stir Welding (FSW) Parameters on Strain Hardening Behavior of Pure Copper Joints, *Mater. Des.*, 2012, **35**, p 330
21. ASTM Int., *Standard Practice for Calculation of Corrosion Rates and Related Information from Electrochemical Measurements* 1, 2015
22. A.K. Lakshminarayanan and V. Balasubramanian, Use of DL-EPR Test to Assess Sensitization Resistance of AISI 409M Grade Ferritic Stainless Steel Joints, *J. Mater. Eng. Perform.*, 2013, **22**, p 2293